



Article

Real-Size Reconstruction of Porous Media Using the Example of Fused Filament Fabrication 3D-Printed Rock Analogues

Alexander A. Oskolkov ^{1,*}, Alexander A. Kochnev ² , Sergey N. Krivoshchekov ²  and Yan V. Savitsky ²

¹ Department of Welding Production, Metrology and Technology of Material, Perm National Research Polytechnic University, 29 Komsomolsky Prospect, Perm 614990, Russia

² Department of Petroleum Geology, Perm National Research Polytechnic University, 29 Komsomolsky Prospect, Perm 614990, Russia; sashakoch93@gmail.com (A.A.K.); krivoshchekov@gmail.com (S.N.K.); yansavitsky@pstu.ru (Y.V.S.)

* Correspondence: oskolkov.w@yandex.ru

Abstract: The multi-scale study of rock properties is a necessary step in the planning of oil and gas reservoir developments. The amount of core samples available for research is usually limited, and some of the samples can be distracted. The investigation of core reconstruction possibilities is an important task. An approach to the real-size reconstruction of porous media with a given (target) porosity and permeability by controlling the parameters of FFF 3D printing using CT images of the original core is proposed. Real-size synthetic core specimens based on CT images were manufactured using FFF 3D printing. The possibility of reconstructing the reservoir properties of a sandstone core sample was proven. The results of gas porometry measurements showed that the porosity of specimens No.32 and No.46 was 13.5% and 12.8%, and the permeability was 442.3 mD and 337.8 mD, respectively. The porosity of the original core was 14% and permeability was 271 mD. It was found that changing the layer height and nozzle diameter, as well as the retract and restart distances, has a direct effect on the porosity and permeability of synthetic specimens. This study shows that porosity and permeability of synthetic specimens depend on the flow of the material and the percentage of overlap between the infill and the outer wall.



Citation: Oskolkov, A.A.; Kochnev, A.A.; Krivoshchekov, S.N.; Savitsky, Y.V. Real-Size Reconstruction of Porous Media Using the Example of Fused Filament Fabrication 3D-Printed Rock Analogues. *J. Manuf. Mater. Process.* **2024**, *8*, 104. <https://doi.org/10.3390/jmmp8030104>

Academic Editor: Chao Yang

Received: 19 April 2024

Revised: 3 May 2024

Accepted: 13 May 2024

Published: 17 May 2024



Copyright: © 2024 by the authors. Licensee MDPI, Basel, Switzerland. This article is an open access article distributed under the terms and conditions of the Creative Commons Attribution (CC BY) license (<https://creativecommons.org/licenses/by/4.0/>).

Keywords: 3D printing; FFF; additive manufacturing; reservoir rocks; lithological and petrophysical properties; reservoir properties; synthetic core; computed tomography; porous media; process parameter control

1. Introduction

The study of void space structure, porosity, permeability, mechanical, and other rock properties is an integral part of oil and gas reservoir development design. As a rule, the number of core samples for research is limited, and the core size is not comparable with the scale of the oil and gas formation. Therefore, the study of possibilities to create synthetic core specimens (replicas) for conducting a series of multi-scale studies, as well as for transition to other scales, is of high relevance.

The vigorous development of additive manufacturing in combination with other technologies (computed tomography (CT), electron microscopy, etc.) provides an opportunity to reconstruct the complex internal structure of rock void space for its subsequent experimental study. The additive manufacturing of synthetic core specimens often presents with a number of problems related to the clogging of specimen pores with expendable material, inconsistency between petrophysical and mechanical properties of specimens, physical and chemical properties of expendable materials, and rock properties [1–5]. The reasons for a mismatch between the internal structure of synthetic specimens and their originals lie in the accuracy of tomography scanners and the resolution of CT images, errors in the conversion of CT images into digital models, peculiarities of different 3D printing technologies (resolution of 3D printers, etc.), and peculiarities of slicers (software for slicing

the digital model into layers, scanning the layer, and creating a control program for the 3D printer).

3D printed specimens are divided into two main categories for a variety of research purposes: synthetic core for mechanical testing and permeability and petrophysical studies, and various physical models, e.g., those for the purposes of mining engineering [3,6–12]. Petrophysical properties of different types of sandstones are discussed, inter alia, in [13–18], and various methods and results of measuring core properties are also described. Three-dimensional printing technologies reduce the cost of core sampling, preparation, and testing.

Thus, further study of 3D printing technologies is required to determine a process that would be most appropriate for core synthesis. Investigation of the influence of the printing process parameters on the petrophysical, mechanical, and other properties of synthesized specimens may be insightful in achieving control of these properties. The research may also tackle creating new 3D printing technologies using natural materials or mixtures based on them.

Presently, additive manufacturing technologies are used in various high-tech industries such as architecture, construction, automotive and aerospace, medicine, and geoscience [19–21]. Any additive manufacturing or 3D printing process involves creating a product by bonding some material layer by layer. The material for 3D printing can be polymers (thermoplastics and photopolymers), composites, metals, ceramics, quartz sand, gypsum, and others [19,20,22].

The main 3D printing technologies currently considered for core reconstruction purposes are selective laser sintering (SLS), stereolithography (SLA/DLP/LCD), PolyJet/MultiJet, fused filament fabrication (FFF), Binder Jetting (BJ), Color Jet Printing (CJP), selective laser curing (SLC), and others.

1.1. Determination of Rock Properties Affecting the Accuracy of Core Reconstruction by Means of 3D Printing: Identification of Similarity Criteria

Highly relevant areas of research include the study of materials for 3D printing of rocks, as well as the study of the possibilities to reproduce rock properties and determining the criteria of the similarity of synthetic specimens to the original rock [23,24].

Terrigenous rocks appear to be more reproducible than carbonate rocks for core reconstruction by 3D printing [9]. As a rule, terrigenous reservoirs are composed of sandstones with admixtures of siltstones, clays, etc. Such rocks have a much more homogeneous lithological compositions and properties [25]. Several sources describe the printing of carbonate rock specimens [26]. The resulting synthetic specimens do not replicate the properties of the original rock but enable visualization of large caverns and fractures within the specimens [27].

In a printed specimen, the primary similarity criteria are its dimensions, diameter and height, the external texture of the specimen, and its mass. These must be consistent with the original core sample [28].

In the studies [29,30], it is noted that the main similarity criteria are associated with the reconstruction of the internal structure of the core, namely porosity, permeability, and density. In article [31], the authors discuss the results of the study of petrophysical properties of specimens manufactured using SLA and PolyJet technology. In [6], the potential application of 3D printing technology in rock mechanics is considered. In [32], the authors emphasize the need to reconstruct porosity to make laboratory testing of synthetic specimens useful.

One of the most important similarity criteria is rock permeability, but so far this criterion has not been reproduced with sufficiently high accuracy [15]. The possibility to reconstruct permeability would be essential for the design of reservoir developments, e.g., for testing of various technologies for enhanced oil recovery, bottom-hole treatment, conformance control, etc.

Wettability also has a significant impact on development efficiency. Wettability has a direct effect on reservoir properties, residual water and oil saturation of rocks, displacement

coefficient, and relative permeability [33]. In [34], permeability and wettability were investigated to characterize the filtration properties of the printed specimens.

When preparing mixtures based on natural components as a material for 3D printing, one possible similarity criterion would be the particle size distribution [35]. The particle size distribution shows the relative content of particles of different sizes in a rock or mixture, regardless of chemical or mineralogical composition. Ideally, cumulative curve plotting is used to compare the materials of the original rock and the synthetic specimen to estimate the percentage of different diameter particles in the rock [36,37].

Particle size analysis is used to evaluate the conditions of rock formation and its genetic characterization [38], making it relevant in the preparation of the material for printing of synthetic specimens. However, in order to evaluate the particle size distribution of the core, it must be destroyed, which is not acceptable in studying its properties. At the same time, additional plug core samples or remnants of the full-sized core from which a plug core sample is made can be used for this purpose. Study [28] determines the average diameter (D50) of the grains of original rock by microscopy and uses artificial sand with the same diameter for printing.

Some of the studies are focused on the mechanical properties of the rock [34]. The uniaxial compressive strength, Young's modulus, friction angle, Poisson's ratio, and Hoek–Brown criterion are used as similarity criteria for mechanical properties [15,39]. Study [6] considers potential application of 3D printing technology in rock mechanics.

According to the literature, regardless of the printing material, the primary similarity criteria are porosity and permeability, which determine the internal structure of the specimens. Particle size distribution, wettability, residual saturation, and mechanical properties are related to the specimen material, so it makes sense to reconstruct them after reliable reconstruction of the internal core structure. The objective of this stage of research is to study the possibility of reconstructing the porosity and permeability of the core by means of 3D printing technologies.

1.2. Possibilities of Reconstructing Rock Porosity and Permeability Using Modern 3D Printing Technologies

Study [40] addresses the task of printing a synthetic soil specimen on the basis of CT images in order to reconstruct pore channels, enabling filtration. Instead of printing the entire digital model of the core, the authors focused on printing its central part. When printing with polyamide (PA) using SLS technology, the internal structure of the specimen was highly consistent with the core. Both conductive channels were reconstructed. When alumide (AL) was used as a printing material, only one conductive channel was reconstructed. This difference may indicate the need to vary the technological parameters of printing depending on the material. The authors noted that 60–80% of the pores were clogged by the expendable material. During filtration studies, the specimens were found to be impermeable to water.

PolyJet and SLA technologies were also used to create a synthetic soil specimen in [40]. As a result of 3D printing using PolyJet technology, it was possible to reconstruct both conductive channels, but the pore channel diameter decreased, and 5% of pores were found to be clogged with the expendable material. During filtration studies, the specimen was impermeable to water. SLA printing enabled the reconstruction of only one conductive channel, but the specimen appeared to be permeable to water.

In [16], PolyJet technology was used to create a synthetic specimen of basalt rock based on CT images. The authors selected a core with large diameter pores of 100 μm and larger. Gas porometry results showed that a specimen with a porosity of 24.9% was obtained, against 25.4% of the core.

In a number of works, the upscaling of models created on the basis of CT images was used to reconstruct the internal structure of rocks using 3D printing methods. A small segment was extracted from a digital core model, and then it was enlarged (scaled up) by 5 to 60 times (or the entire model was scaled up). The scale was chosen by the authors based

on the technical capabilities (resolution) of the 3D printer and tomograph. For instance, in [41], 3D printing of enlarged core models using SLA technology yielded specimens with porosity between 10.9 and 11.6%, against 12.7% of the core. In [42], for printing the specimen, the authors scaled up a portion of the core model. PolyJet-manufactured specimens manifested 2% lower porosity than the core (21.6%) as well as a reduction in pore channel diameter. In [31], the authors also scaled up sandstone model segments for 3D printing using PolyJet and SLA technologies. The best specimen manufactured using PolyJet technology manifested a porosity of 18.6%, permeability of 851 mD, and an effective porosity of 6.1%, which the authors attribute to pore clogging by the expendable material (the core had a porosity of 24.8%, permeability of 1025 mD, and effective porosity of 19.8%). The SLA-manufactured specimen manifested a porosity of 7.45% and an effective porosity of 5.22% compared to 10.02% and 6.25% of the core, respectively. A similar study was performed in [29,43], where specimens of enlarged segments of carbonate rock and sandstone models were produced using PolyJet and SLA technologies. The results of the porosity and permeability measurements showed high consistency between specimens and cores (porosity deviation up to 1%, permeability up to 50%).

Works [44] and [45] discuss the results of printing rock specimens with upscaling. In study [44], the specimen was printed using DLP technology with a photopolymer composite. The specimen porosity ranged from 18.2% to 18.9%, versus 22.64% of the core. At the same time, the porosity of the digital model was 21.83%. This is indicative of the presence of an error in the conversion of the CT image into a digital model. In research [45], LCD printing results showed a 7.5% decrease in porosity of the specimen compared to the core. Upscaling has also been used in a number of other works [46,47].

In research [10], the authors manufactured real-size synthetic sandstone specimens (core model based on CT images) using several 3D printing technologies. A study of the properties of the SLA-manufactured specimen showed a porosity of 23% and permeability of 96 mD. The porosity and permeability of the core were 20% and 100 mD, respectively.

The specimen in study [10], manufactured from gypsum powder using CJP technology, manifested a porosity of 22% and permeability of 110 mD. Measurements were performed using gas porometry. The studies of this specimen were continued by the authors in [26], where the porosities of the core and the gypsum specimen were re-measured. The mercury porometry results showed porosity values of 28.7% for the specimen and 14.3% for the core.

The authors of [48] present the results of the 3D printing of sandstone specimens using CJP technology with upscaling of the core model created on the basis of CT images. The measurements were performed using mercury porometry. The resulting porosity of the specimens ranged within 28.3 to 37.5%, and the permeability within 349.6 to 443.2 mD. Meanwhile, core porosity and permeability measurements through digital analysis (DA) yielded values of 12.6% and 251.4 mD. The authors also provide reference data on sandstone properties (11% and 454.7 mD) for comparison.

Thus, in studies [10,26,48] there is a significant difference between the results of measurements using gas and mercury porometry. At the same time, the authors of [17] manufactured a gypsum powder specimen using CJP technology based on a digital model of a solid cylinder, which matched the standard core in size and shape. The porosity of the specimen was measured by gas (28.86%) and mercury (27.9%) porometry and digital analysis of CT images of the specimen (32.66%).

In research [34], the authors present the results of the study of the porosity and permeability of synthetic specimens manufactured using BJ and SLC technologies based on the solid cylinder model. BJ technology is similar to CJP. The results of printing a gypsum powder specimen (similar to CJP) using BJ technology were shown. The porosity of the gypsum specimen was 9.2%. The silica sand specimen made using SLC technology manifested a porosity of 40.1% and a permeability of 9840 mD. The specimen made of silica sand using BJ technology manifested a porosity of 52.1% and permeability of 12,580 mD. The porosity and permeability of the reference sandstone were 24.6% and 3960 mD, respectively.

Study [49] discusses the anisotropy of properties of specimens manufactured using BJ technology based on the solid cylinder model. The authors took two specimens and extracted from each of them two segments of different diameters (6 mm and 12 mm) in the vertical (38 mm long) and horizontal (28 mm long) directions. The results of porosity measurements showed that it did not depend on the direction in which the segment was extracted. However, the porosity of both segments with smaller diameters (6 mm) was 48% while the porosity of the larger diameter segments (12 mm) was 36–39%, indicating the existence of a scale effect in measuring the porosity of rock samples. The porosity of the reference sandstone was 16.2%.

A number of studies discuss ways to reduce the porosity of synthetic specimens manufactured using the BJ process. The control of printing parameters in the BJ process, such as binder volume fraction [14,32,50], layer height, and particle size distribution of the expendable material (quartz sand) in research [51] allowed them to obtain specimens with different internal structures. In [14,50], the authors discuss the results of permeability and porosity measurements for specimens with different percentages of saturation with polymer binder. For the specimen with 10% binder volume fraction, the porosity was 48% and permeability 1800 mD, and for the specimen with 20% binder volume fraction, 36% and 1000 mD, respectively.

The authors of [51] showed that changing the particle size distribution of the sand mixture (ratio of coarse to fine fractions) reduces the porosity of synthetic specimens from 49.3% (100% fine fraction) to 40.5% (100% coarse fraction) at a layer height of 200 μm . At the same time, reducing the layer height from 400 to 200 μm leads to a decrease in porosity of the specimens from 48.3% to 41.2% when using only coarse sand.

In article [30], the reduction of the porosity of synthetic specimens manufactured using BJ technology was achieved by increasing the diameter of the roller (the mechanism that feeds the expendable material), which resulted in the compaction of the material during the printing process. The compaction of the material with the help of a larger roller allowed them to achieve a decrease in porosity of the specimens from 51% to 45.3% (for 100% fine fraction) and from 44.4% to 40.2% (for 100% coarse fraction) at a layer height of 350 μm .

Another appealing area of research is large-format construction 3D printing technologies using concrete mix extrusion (3DCP) [52,53]. Study [54] is dedicated to multilayer structures made of concrete mixtures. Mercury porometry measurements showed that the porosity of the extracted segments of the multilayer structures was 23%. At the same time, the effective porosity was 17.6%. The results of digital CT image analysis indicated 32.6% porosity. Studies [55,56] present the results of printing specimens based on a solid cylinder model using extruded concrete mixtures and clay.

The 3D printing of synthetic rock specimens by material extrusion is also used in FFF technology. In works [57–59], the authors propose an approach to 3D printing of synthetic specimens with a given porosity and permeability by forming lattice structures of various shapes. The specimens are printed on the basis of digital models of a solid cylinder or cube, and the lattice structure is formed by varying the parameters of depositing the layer with material filament. The authors note that printing lattice structures produces stray porosity caused by undesired (stray) gaps between neighboring filaments of thermoplastic material and discontinuities within the filaments.

The authors of [46] use FFF 3D printing technology to reproduce the internal structure of sandstone but note that FFF 3D printers have low resolution. To print the specimen, the authors use upscaling of a digital model built on the basis of the sandstone CT images. The study of the specimen structure showed that the FFF 3D printing process can generate pores smaller than the resolution of the 3D printer.

Authors of [10] manufactured real-size sandstone specimens (based on CT images) using FFF technology. Gas porometry results showed that the PLA specimen had a porosity of 18% and a permeability of 150 mD, versus 20% and 100 mD of the core. ABS and CPE specimens manifested porosities of 15% and 28% and permeabilities of 60 mD and 80 mD, respectively. The authors also cite the results of mercury porometry, which showed a core

porosity of 14.3% [26]. Unfortunately, in study [10] there is no information regarding the process parameters of FFF printing and the layer depositing parameters.

In research [40], one of the synthetic soil specimens was manufactured from ABS plastic using FFF technology. The ABS specimen had six times higher macroporosity than the original, as well as a large number of isolated micropores. The CT image of the internal structure of the specimen shows that the main reason for high macroporosity is the stray gaps between neighboring filaments of the material, and the specimen itself has a typical lattice structure similar to those shown in [57–59]. The authors do not provide information about the process parameters of printing. The CT image also shows conductive channels. The ABS specimen is the least prone to the pore clogging problem among all specimens. During the filtration studies, only the specimens made by FFF and SLA technologies appeared to be permeable to water.

In [60], the authors manufactured a sandstone specimen using FFF 3D printing technology from HIPS (high impact polystyrene) plastic with 5–20% calcite filling. The authors used core model upscaling (based on CT images) to create the specimen. As a result, the specimen with 5% calcite filling showed a porosity of 28%, and with 15% calcite, a porosity of 33% was seen, against 25% of the core. The deviations may be due to the low printing resolution (layer height 0.2 to 0.3 mm, nozzle diameter 0.5 mm) with calcite crystal size ranging from 60 to 90 μm.

Based on the appearance of the specimens, CT results and the authors’ comments, it can be concluded that in [40,46,57–60], a typical FFF 3D printing strategy of layer filling was generally used: a lattice-like infill of the solid phase of the model and an outer wall that is generated at the solid phase and void space boundaries both outside and inside the digital model for each layer.

Table 1 contains the results of the studies of porosity and permeability of synthetic rock specimens obtained by different 3D printing methods.

Table 1. Results of studies of porosity and permeability of synthetic rock specimens.

3D Printing Technology	Authors	Porosity, %		Permeability, mD	
		Core	Specimen	Core	Specimen
SLA	[10]	20	23	100	96
	[31] *	10.2	7.45	14	-
	[41] *	12.7	11.6	-	-
DLP	[44] *	22.6	18.9	-	-
PolyJet	[31] *	24.8	18.6	1000	850
	[42] *	21.6	19.6	-	-
	[16]	25.4	24.9	-	-
	[29] *	6.7	6.1	1590	1276
BJ	[34]	24.6	52.1	3950	12,580
	[49]	16	36	-	-
CJP	[10,26]	14.3	28.7	100	110
	[48] *	12.6	37.5	251	440
	[48] *	12.6	28.4	251	349
	[31,48] *	12.6	30.3	251	419
SLC	[34]	24.6	40.1	3950	9840
FFF	[10]	20	18	100	150
	[10]	20	12	100	62
	[10]	20	15	100	60
	[10]	20	28	100	80
	[60] *	25	33	-	-
	[60] *	25	28	-	-

* digital core models were scaled up.

Synthetic rock specimens created by 3D printing technologies using natural materials (BJ, CJP, SLC) exhibit porosity values higher than those of the original rock. There are studies devoted to 3D printing using composite materials [44,45,60]. The specimens manufactured using PolyJet, SLS, and SLA 3D printing technologies are characterized by a decrease in pore space and a partial occlusion by expendable materials [16,31,40,42]. The latter problem has also been reported for CJP technology [48]. Many authors apply upscaling of core models, justifying it by citing the insufficient resolution of the existing 3D printers (PolyJet, SLA, CJP, FFF). At the same time, using different approaches to processing CT results and adapting digital models for 3D printing, selecting a suitable rock for printing, and varying the 3D printing parameters allowed researchers, in a number of cases, to obtain results in which the synthetic specimens were highly consistent with the natural core.

As was mentioned, the multi-scale study of rock properties is a necessary step in the planning of oil and gas reservoir developments. The amount of core samples available for research is usually limited, and some of the sample can be distracted. The investigation of core reconstruction possibilities is an important task.

This work is devoted to the real-size reconstruction of sandstone cores using FFF technology. This technology offers the vastest range of possibilities to customize printing parameters. Varying the printing parameters can help control the properties of synthetic specimens and reproduce the internal structure of the core sample with sufficient accuracy.

An approach to the real-size reconstruction of porous media with given (target) porosity and permeability by controlling the parameters of FFF 3D printing using CT images of the original core is proposed.

2. Materials and Methods

The basic concept of creating synthetic specimens (replicas) of rocks is as follows: scanning the core using X-ray computed tomography, creating a three-dimensional model of the core in specialized software products, and printing the model on a 3D printer [26,40,46]. The current references generally offer one common approach to reconstructing digital models from CT images for 3D printing [46,48,49,61,62].

2.1. Core Selection for 3D Printing: Geological Description

The core sample from a well of one of the fields of the Volga-Ural oil and gas province was selected for the study. The core sampling interval belongs to an oil-saturated reservoir of Visean age. The sample is composed of coarse-to-medium-grained sandstone with porosity of 14% and permeability of 271 mD. The plug core dimensions are 30 mm in diameter and 55 mm in height.

Core sample tomography was performed to evaluate the void space structure. A Nikon Metrology XT H 225 tomograph was used. The radiation source is an open microfocus gun, X-ray gun current is 0–1 mA, and rated power is 225 W. The operating voltage difference of the unit is from 30 to 225 kV. The external radiation is not more than 1 μ Sv/h at a distance of 5 cm. The dimensions of the digital detector are 406 by 292 mm and the detector resolution is 2304 \times 3200. The system resolution is up to 1 μ m. The hot wire is tungsten; the target is tungsten, reflective; external water cooling is used. The system is equipped with a 5-axis manipulator with a maximum load of 15 kg. The Nikon Metrology Inspect-X Software 3.0 is used. [63,64].

Figure 1 shows the results of the 3D reconstruction of the sandstone core.

The sandstone (Figure 1) is a mainly homogeneous void space due to primary porosity. There is no change of lithotypes. Intergranular supercapillary and capillary porosity is observed throughout the core.

The UltraPoroPerm-500 Gas Permeameter–Porosimeter was used to determine the effective porosity and absolute permeability of the core and manufactured synthetic specimens. This is a system combining the functions of two devices in a single integrated module that enables the measurement of specific gas permeability as well as the Klinkenberg permeability, as well as core porosity under pressure. The open porosity coefficient

on a standard size core was determined by the gas volumetric method. The determination of porosity by gas-volumetric method is based on the Boyle–Mariotte law. The method determines the volume of the core solid phase and its external volume. The void volume is defined as the difference between the external volume of the core and the volume of its solid phase. The absolute gas permeability coefficient was determined by the method of stationary gas filtration. The method determines the constant (stationary) velocity of gas filtration through the core in a linear direction under the effect of a pressure difference. In the case of stationary filtration, the velocity is determined by the known volume of gas passing through the core over a fixed period of time at a constant pressure difference. The absolute error of the porosity measurement is up to 1%.

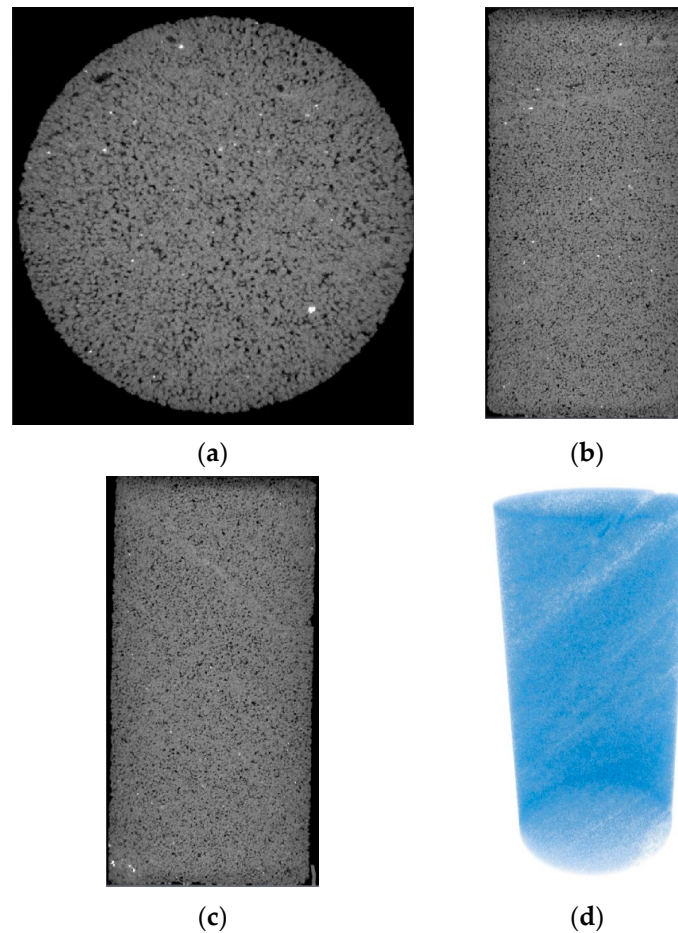


Figure 1. Tomogram of sandstone core: (a) section along XY axis; (b) section along XZ axis; (c) section along YZ axis; (d) 3D view of void space.

2.2. Creation of a Digital Core Model Based on Computed Tomography Results and Adaptation of the Model for 3D Printing

In a number of studies, the authors report the insufficient resolution of 3D printers to accurately reproduce the pore space of the core due to the small pore size. However, the printing process directly reproduces the skeleton of the core model. It can be assumed that the size of reproducible pores in a synthetic specimen can be as small as desired. Thus, not only the pore size but also pore spacing matters.

The distance between neighboring pores may be too small to be reproduced given the available 3D printer resolution. If such a solid segment of the digital model is recognized by a slicer, then in the process of printing, the extruded material will block some of the area of the adjacent pores, resulting in an undesired reduction of the pore space. Depending on the slicer that is being used, either holes or solid segments of the model smaller than a certain

size may be neglected when scanning a layer. In the first case, an undesired reduction, and in the second case, an undesired expansion of the pore space will occur.

To minimize the effects associated with undesired pore space reduction or expansion, and to simplify the generation of the layer filling trajectory in FFF 3D printing, isolated pores were filtered out by size. Filtering out isolated pores smaller than a certain size provided a more homogeneous environment and did not affect the permeability of the digital core model.

CT images were prepared with isolated pores of at least 50, 100, and 150 μm and without filtration. Isolated pores were not removed completely to preserve the internal structure of the core. The last step is to generate a digital model based on the CT image and further simplify the model while preserving the pore size. The Avizo Fire 7 software was used to process the tomography results and create and adapt the digital core model.

The digital core model is imported into the slicer. Two slicers were used to generate the layer filling trajectories and set the values of the FFF 3D printing parameters. The Simplify3D slicer ignores solid segments of the model smaller than 100 μm . The Cura Ultimaker slicer ignores holes in the model smaller than 100 μm .

Next, the control program is transferred to the 3D printer. The specimens were printed using FFF 3D printer model p902 manufactured by Flyingbear 3D Technology Co., Ltd. (Zhejiang, China). The resolution of the FFF 3D printer depends on the positioning accuracy (5 μm in XY axis, 2 μm in Z axis), nozzle bore diameter (0.1–1 mm), and layer height (0.05–5 mm). A PLA semi-crystalline thermoplastic material in the form of a white filament with a diameter of 1.75 mm produced by PrintProduct (St. Petersburg, Russia) [65] was used for printing. The PLA glass transition temperature is about 50–65 $^{\circ}\text{C}$ [66–68], and the temperature of complete melting of the crystalline phase is about 150–165 $^{\circ}\text{C}$ [66–68].

FFF 3D printing technology involves creating a product layer by layer by fusing together filaments of thermoplastic material that are extruded through a hot nozzle. The first layer of material is deposited to the platform.

Prior to printing, the platform and extruder are heated to the specified temperatures T_{pl} and T_{ext} , respectively. Next, a thin layer of adhesive solution (polyvinylpyrrolidone (PVP)-based glue) is deposited on the platform to ensure the secure attachment of the specimen to the platform during the printing process.

3. Results and Discussion

To verify the hypothesis about the possibility to reconstruct the pore space of the core in real-size by FFF 3D printing, a series of PLA plastic specimens was manufactured. The influence of the different process parameters of FFF 3D printing on the porosity and permeability of the specimens was studied.

3.1. FFF 3D Printing Process Parameters

As a rule, in the FFF 3D printing process, the platform temperature is maintained above the glass transition temperature of the plastic, which provides better adhesion of the first layer of the material to the platform. Keeping the plastic in a highly elastic state during the long printing process leads to the compaction of the lower layers of the product and slow passing of the thermoplastic filament coalescence process [66,69]. To minimize the undesired pore space reduction caused by the said effects, after depositing the first layer of material, the platform temperature T_{pl} was reduced from 70 to 40 $^{\circ}\text{C}$. Adhesion of the part to the platform during the printing process was ensured by an adhesive solution.

Nozzles with bore diameters of 0.25 and 0.3 mm were chosen to print the specimens. The corresponding line width l_{xy} (0.25 or 0.3 mm) was software-specified during the slicing of the digital core model, which determined the print resolution in the XY plane. The layer height l_z was set to 0.07 or 0.1 mm, which determined the print resolution in the Z axis. Core specimens were printed at various combinations of layer height l_z and line width l_{xy} .

One of the steps in calibrating a 3D printer to prepare for the printing process is determining the material flow (extrusion multiplier, dimensionless units), which defines

the volumetric flow rate of a particular material. By changing the material flow, it is possible to adjust the filament width of the material at a constant filament height (layer height l_z). At the same time, the filament width can deviate to a greater or lesser extent from the software-specified line width l_{xy} . Thus, for certain values of flow and l_{xy} line width, both gaps and overlaps between neighboring material filaments can be provided. When printing the specimens, the material flow varied from 0.63 to 0.98. In the Cura Ultimaker and Simplify3d slicers, the ways to calculate the material flow (extrusion multiplier) are slightly different.

The thermoplastic material extrusion temperature T_{ext} was set as low as possible to minimize the effects associated with spontaneous flow of plastic from the nozzle during travel movements. Such stray flows of plastic may cause the pores to become clogged. The temperature T_{ext} reduction promotes faster solidification of the deposited material and prevents deformation of the previous material layer due to overheating [70,71]. The latter may lead to a disruption of the internal structure of the specimen and pore clogging. Insufficiently high T_{ext} may result in a low bond strength between layers [71–75] or an interruption in the material extrusion process. During printing of the specimens, T_{ext} increased from 180 to 195 °C simultaneously with an increase in the material volumetric flow rate.

The linear printing speed was selected based on the possibility to extrude material at minimum T_{ext} and minimum material flow. A change in the linear printing speed leads to a change in the extrusion speed, i.e., the volumetric material flow rate. The print speed of the 0.3 mm nozzle was 40 mm/s, and that of the 0.25 mm nozzle was 35 mm/s.

The specimens were printed with a layer filling strategy similar to [40,46,57–60]. Lattice infill was used for the solid phase of the digital model. The layer filling density was software-specified to 100%. The lattice filling direction was changed from layer to layer according to the specified angles: 45° / –45°. The outer wall was generated at the solid phase and void space boundaries both outside and inside the model for each layer. When printing the specimens, the software-specified percentage of overlap between the infill and the outer wall varied from 20 to 50%. The percentage of overlap determines the distance between the infill and the outer wall, and thus the size of gaps between them.

When printing the specimens, plastic retracts were used at travel movements to minimize the spontaneous flow of plastic out of the nozzle. A retract suggests pulling the plastic back into the extruder by a certain distance. In some cases, when the travel movement was completed and printing was resumed (restarted), 4 to 10% more plastic was fed into the nozzle than was pulled back. Increasing the feed (restart distance) of plastic after a retract helps compensate for the residual effect of stray plastic flow from the nozzle. The retract distance was varied from 0.2 to 0.5 mm. The restart distance was varied from 0 to 0.54 mm. The retraction speed was 70 mm/s.

3.2. Results of FFF 3D Printing of Synthetic Core Specimens

PLA specimens were manufactured based on the results of computed tomography and the obtained digital core model. Preparation of the digital core model for 3D printing was performed using Cura Ultimaker and Simplify3d slicers. Core models with isolated pores of at least 100 µm and 150 µm were selected for printing. The external appearance of the core (sandstone No.10) and manufactured specimens is presented in Figure 2.

Table 2 presents the process parameters and results of the printing of the specimens prepared in Cura Ultimaker slicer. Taking into account the internal program limitations of the Cura Ultimaker slicer, a model with isolated pores of at least 100 µm was selected for printing. When printing specimens No.6, No.10, No.11, No.18, and No.26, plastic retracts with a distance of 0.4 mm were used. At resumption (restart) of printing, no additional volume of plastic was fed into the nozzle. The retract distance (0.4 mm) to which the plastic was pulled back was equal to the restart distance (0.4 mm), i.e., to the length of the filament that is fed into the nozzle when the printing process is resumed.



Figure 2. External appearance of the core (sandstone No.10) and synthetic specimens.

Table 2. Process parameters and results of printing PLA specimens prepared in Cura Ultimaker slicer.

Specimen No.	Porosity, %	Permeability, mD	Material Flow, d.u.	Extrusion Temperature, °C
6	22.6	881.3	0.81	180
10	18.7	411.7	0.86	180
11	15.4	664.6	0.93	190
18	16.5	502.5	0.93	190
26	8	0.03	0.98	190

Specimens No.6, No.10, No.18, and No.26 were produced at the maximum printing resolution with a combination of nozzle diameter (software-defined line width) $l_{xy} = 0.25$ mm and layer height $l_z = 0.07$ mm. Specimen No.11 was produced with $l_z = 0.1$ mm.

Based on the measurements, the porosity of specimen No.6 was 22.6% and the permeability was 881.3 mD, against 14% and 271 mD of the original core. The data presented in Table 2 shows that a gradual increase in material flow helped reduce the porosity and permeability of the specimens to 16.5% and 502.5 mD (specimen No.18), respectively. However, further increase in material flow resulted in the porosity and permeability to drop to 8% and 0.03 mD (specimen No.26). To explain this fact, Figure 3 shows the CT results for specimen No.6.

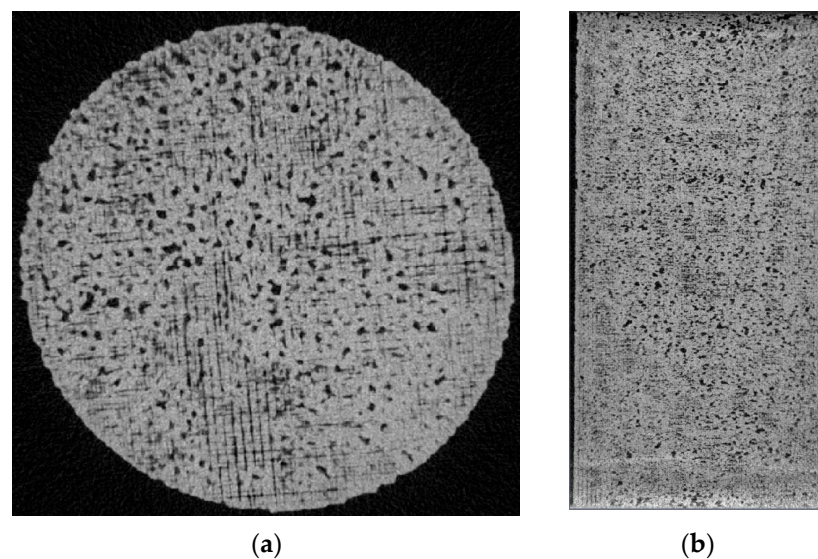


Figure 3. Results of computed tomography of sectioned specimen No.6: (a) section in the XY plane ($z = 477$ mm); (b) section in the XZ plane ($y = 248$ mm).

Figure 3 demonstrates the presence of stray gaps between neighboring material filaments (black lines are gaps, white lines are filaments). Thus, the void space inside the specimen is formed not only by reconstructing the pore space of the core model, but also by stray gaps in the lattice structure of the model's solid phase infill. A similar result was obtained by the authors of [40]. A gradual increase of material flow in specimens No.10, No.11, and No.18 contributed to the reduction of gaps and pore size. When the stray gaps were eliminated in printing specimen No.26, the effective porosity and permeability values were found to be extremely low. Unfortunately, we were unable to achieve the goal of the study with the Cura Ultimaker slicer.

The results of 3D printed PLA specimens prepared in Simplify3d slicer were divided into four tables for different combinations of l_{xy} and l_z parameters. Figure 4 shows a closeup of the core (sandstone No.10) and specimen No.7.

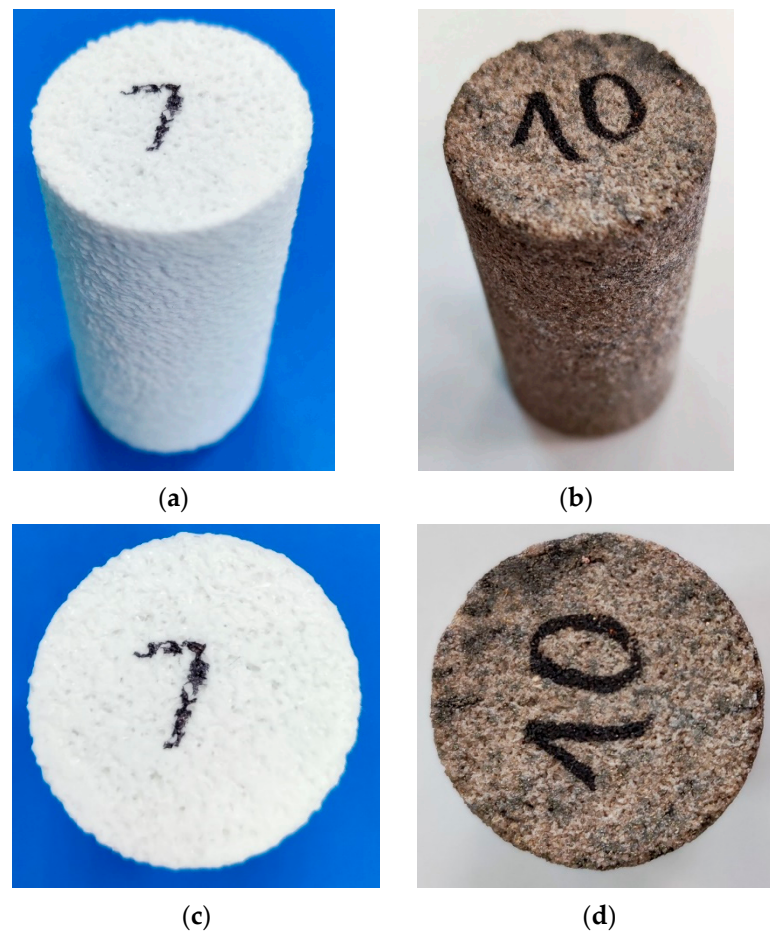


Figure 4. External appearance of the core (sandstone No.10) and specimen No.7 prepared in Simplify3d slicer: (a) specimen No.7, side view; (b) core, side view; (c) specimen No.7, top view; (d) core, top view.

Table 3 presents process parameters and printing results for specimens No.4, No.5, No.12, and No.23 with maximum printing resolution at the combination of $l_{xy} = 0.25$ mm and $l_z = 0.07$ mm. Digital core models with minimum size of isolated pores of 150 μm and 100 μm were used to print specimens No.4 and No.5, respectively.

According to the measurement results, specimens No.4 and No.5 have almost the same porosity (44.2% and 44.5%). For this reason, a digital core model with a minimum isolated pore size of at least 150 μm was used to print the other specimens. A gradual increase of material flow from 0.68 to 0.85 and the percentage of overlap between the infill and the outer walls from 20% to 25% reduced the porosity of the specimens from 44.2% to 27.4% and the permeability from 45,209 mD to 2142 mD. The reduction in void space in response

to the increase in the material flow and percentage of overlap was as expected. This effect has also been observed when 3D printing specimens with other l_{xy} and l_z combinations.

Table 3. Process parameters and printing results for specimens prepared in Simplify3d slicer for $l_{xy} = 0.25$ mm and $l_z = 0.07$ mm.

Specimen No.	Porosity, %	Permeability, mD	Material Flow, d.u.	Extrusion Temperature, °C	Overlap, %	Retract/Restart, mm
4	44.2	45,209	0.68	180	20	0.4/0.4
5	44.5	38,757.5	0.68	180	20	0.4/0.4
12	31.9	13,159.7	0.8	185	25	0.4/0.4
23	27.4	2142.9	0.85	195	25	-

Figure 5 shows the results of the computed tomography of specimen No.4. Figure 5 shows stray gaps between neighboring filaments of material similar to specimen No.6 (Figure 3), but the porosity of specimen No.4 is approximately twice higher than that of specimen No.6.

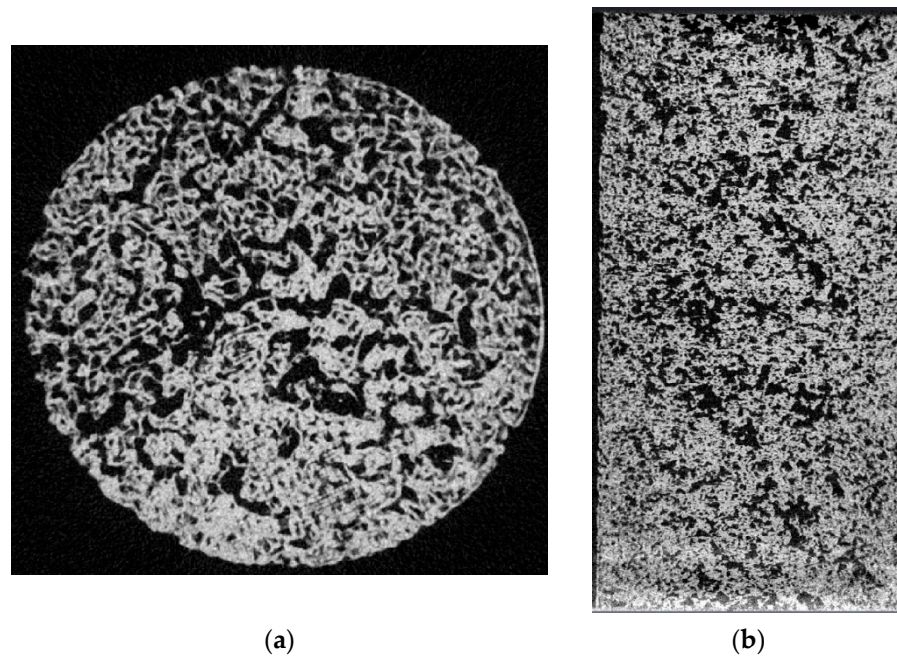


Figure 5. Results of computed tomography of sectioned specimen No.4: (a) section in the XY plane ($z = 477$ mm); (b) section in the XZ plane ($y = 245$ mm).

Table 4 shows the process parameters and printing results for specimens No.2, No.15, No.22, No.28, and No.33 at a combination of $l_{xy} = 0.3$ mm and $l_z = 0.07$ mm.

Table 4. Process parameters and printing results for specimens prepared in Simplify3d slicer for $l_{xy} = 0.3$ mm and $l_z = 0.07$ mm.

Specimen No.	Porosity, %	Permeability, mD	Material Flow, d.u.	Extrusion Temperature, °C	Overlap, %	Retract/Restart, mm
2	31.3	5680	0.63	180	20	0.5/0.52
15	19.7	1267.5	0.75	190	25	0.2/0.22
22	17	300.2	0.8	195	25	0.2/0.22
28	21.3	439.4	0.85	195	25	-
33	18	539.7	0.9	195	25	-

Table 5 shows the process parameters and printing results for specimens No.3, No.13, No.24, and No.29 at a combination of $l_{xy} = 0.25$ mm and $l_z = 0.1$ mm.

Table 5. Process parameters and printing results for specimens prepared in Simplify3d slicer for $l_{xy} = 0.25$ mm and $l_z = 0.1$ mm.

Specimen No.	Porosity, %	Permeability, mD	Material Flow, d.u.	Extrusion Temperature, °C	Overlap, %	Retract/Restart, mm
3	42	-	0.68	180	20	0.4/0.4
13	18.4	1725.8	0.8	185	25	0.2/0.22
24	17.3	851.1	0.85	195	25	0.2/0.22
29	24.1	2372.4	0.9	195	25	-

Table 6 shows the process parameters and printing results for specimens No.7, No.9, No.14, No.21, No.27, No.31, No.32, No.37, No.39, and Nos.42–46 at a combination of $l_{xy} = 0.3$ mm and $l_z = 0.1$ mm.

Table 6. Process parameters and printing results for specimens prepared in Simplify3d slicer for $l_{xy} = 0.3$ mm and $l_z = 0.1$ mm.

Specimen No.	Porosity, %	Permeability, mD	Material Flow, d.u.	Extrusion Temperature, °C	Overlap, %	Retract/Restart, mm
7	32	8131.4	0.63	180	20	0.5/0.52
9	15.6	688.3	0.72	190	20	0.5/0.54
14	20.4	1518.1	0.75	195	25	0.2/0.22
21	18.1	393.7	0.8	195	25	0.2/0.22
27	18.2	525.4	0.85	195	25	-
31	20.1	747.7	0.85	195	20	-
32	13.5	442.3	0.9	195	25	-
37	11.5	335.4	0.85	195	40	-
39	17.5	680.5	0.8	195	40	-
42	10.6	427.2	0.82	195	50	-
43	12.7	418	0.88	195	30	-
44	11.6	341.2	0.87	195	35	-
45	11.9	485.7	0.83	195	45	-
46	12.8	337.8	0.92	195	20	-

The printing of specimens Nos.2–22 and No.24 was performed with plastic retracts in travel movements. Tables 3 and 5 show that in printing specimens No.3, No.4, No.5, and No.12, the plastic retracts were similar to those made in specimens No.6, No.10, No.11, No.18, and No.26 (Table 2). Tables 4 and 6 show that when printing the specimens No.2 and No.7, the retract distance was 0.5 mm, whereas the restart distance was 0.52 mm. That is, when printing was resumed after a retract, 0.02 mm more filament was fed into the nozzle than was pulled back.

When printing specimen No.9, the material flow was increased from 0.63 to 0.72 compared to specimen No.7. At the same time, the restart distance was increased from 0.52 to 0.54 mm (0.04 mm more than the retract). The measurement results showed that specimen No.9 had a porosity of 15.6% and permeability of 688 mD compared to 32% and 8131 mD for specimen No.7, and 14% and 271 mD for the original core. Figure 6 shows the CT results for specimen No.9 and the original core.

Based on the visual analysis of the CT images presented in Figure 6, it was suggested that the total porosity of specimen No.9 is greater than that of the core, and the proximity of the effective porosity and permeability values is caused by the clogging of pores and channels in specimen No.9. This assumption was confirmed by the results of the digital analysis of CT images, according to which the porosity of specimen No.9 was 19%.

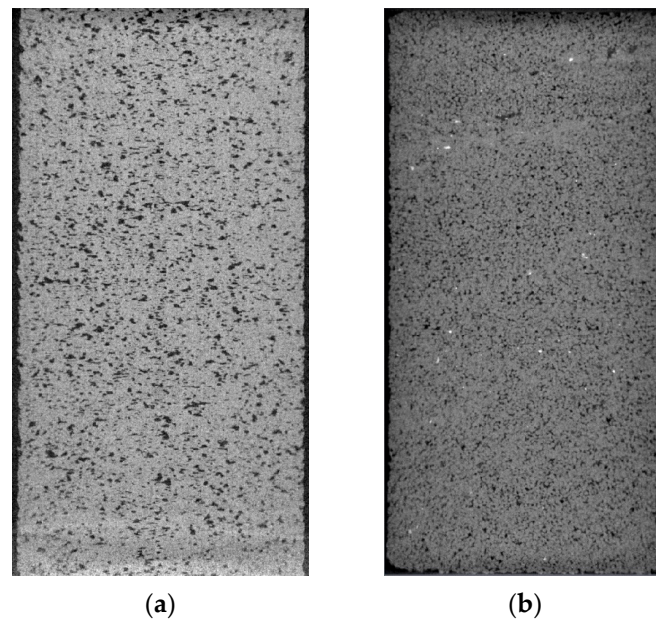


Figure 6. CT results for specimen No.9 and core in section: (a) section of specimen No.9 in the XZ plane ($y = 246$ mm); (b) core section in the XZ plane ($y = 251$ mm).

Further, for specimens in Tables 4–6, the retract distance was reduced to 0.2 mm, and the restart distance was reduced to 0.22 mm. These settings were used when printing specimens No.13, No.14, No.15, No.21, No.22, and No.24 with various combinations of l_{xy} and l_z .

When printing specimen No.14, the material flow was increased from 0.72 to 0.75 and the percentage of overlap from 20% to 25% compared to specimen No.9. Despite this, the porosity and permeability measurements of specimen No.14 showed an increase in porosity from 15.6% to 20.4% and permeability from 688.3 mD to 1518.1 mD compared to specimen No.9. An assumption was made that the reason for the increase in porosity and permeability could be due to the decrease in restart distance. Now, at restart, the nozzle was additionally fed with 0.02 mm of filament instead of 0.04 mm.

When printing specimens No.21, No.22, and No.24, the material flow was increased by 5 units compared to specimens No.13, No.14, and No.15. The expected results were obtained. The porosity of specimen No.21 decreased from 20.4% to 18.1% and permeability from 1518.1 mD to 393.7 mD compared to specimen No.14. The porosity of specimen No.22 decreased from 19.7% to 17% and the permeability from 1267.5 mD to 300.2 mD compared to specimen No.15. The porosity of specimen No.24 decreased from 18.4% to 17.3% and permeability from 1725.8 mD to 851.1 mD compared to specimen No.13.

3.2.1. Three-Dimensional Printing of Synthetic Specimens without Plastic Retracts

The gradual increase in the material flow resulted in the conditions when the material did not have time to warm up to a temperature sufficient for stable extrusion. This problem was solved by increasing the extrusion temperature T_{ext} . At the same time, the operation at low extrusion temperatures ensured the minimization of the stray flow of plastic from the nozzle during travel movements. Considering the assumption made on the basis of comparing specimens No.9 and No.14, retracts were disabled.

When printing specimen No.23, the material flow was increased from 0.8 to 0.85 compared to specimen No.12, and plastic retracts were disabled. The measurement results showed that the porosity of specimen No.23 decreased from 31.9% to 27.4% and the permeability from 13,159.7 mD to 2142 mD. The 4.5% decrease in porosity is comparable to the results of comparing specimens No.21 and No.14, No.22 and No.15, and No.24 and No.13, where the retract settings are the same and only the material flow was changed by 5 units. Thus, to prevent pore clogging due to the stray flow of plastic from the

nozzle during travel movements, it suffices to lower the extrusion temperature T_{ext} to the minimum possible.

When printing specimens No.27, No.28, and No.29, material flow was increased by 5 units compared to specimens No.21, No.22, and No.24, and plastic retracts were disabled. As a result, the porosity of specimen No.27 increased from 18.1% to 18.2% and the permeability from 393.7 mD to 525.4 mD compared to specimen No.21. The porosity of specimen No.29 increased from 17.3% to 24.1% and the permeability from 851.1 mD to 2372.4 mD compared to specimen No.24. The porosity of specimen No.28 increased from 17% to 21.3% and permeability from 300.2 mD to 439.4 mD compared to specimen No.22. Similar increases in effective porosity and permeability were observed when comparing specimens No.14 and No.9.

It can be concluded that at low temperatures T_{ext} , the use of retracts and restarts with increased plastic feed led to the clogging of pores and channels. In other words, as the restart distance increases, the porosity and permeability of the specimens decrease. This explains the results of the comparison of specimen No.9 and the core (Figure 6). In some cases, retracts and restarts with increased plastic feed can be used to control the porosity and permeability of synthetic rock specimens or other porous media.

It should also be noted that an increase in the nozzle diameter or layer height leads to a decrease in porosity and permeability. At a layer height of 0.1 mm, this effect can be observed when comparing specimens No.24 (nozzle diameter 0.25 mm) and No.32 (nozzle diameter 0.3 mm). The porosity of specimen No.24 is 17.3% versus 13.5% for specimen No.32. At a layer height of 0.07 mm, this effect can be observed when comparing specimens No.23 (nozzle diameter 0.25 mm) and No.28 (nozzle diameter 0.3 mm). The porosity of specimen No.23 is 27.4% versus 21.3% for specimen No.28. The effect of layer height can be observed when comparing specimens with a nozzle diameter of 0.3 mm. The porosity of specimen No.27 (layer height 0.1 mm) is 18.2% versus 21.3% for specimen No.28 (layer height 0.07 mm). The porosity of specimen No.32 (layer height 0.1 mm) is 13.5% versus 18% for specimen No.33 (layer height 0.07 mm).

3.2.2. Dependence of Porosity and Permeability of a Synthetic Specimen on Material Flow and Percentage of Overlap

The porosity and permeability of the specimens as a function of material flow and overlap percentage were studied at a combination of $l_{xy} = 0.3$ mm and $l_z = 0.1$ mm. The material flow varied from 0.8 to 0.92 and the percentage of overlap from 20% to 50%. The extrusion temperature was kept constant and equal to $T_{ext} = 195$ °C; the retracts were disabled. Results for printing of specimens Nos.27–46 are given in Table 6.

When printing specimen No.31, the overlap percentage was reduced from 25% to 20% compared to specimen No.27. As a result, the porosity of specimen No.31 increased from 18.2% to 20.1% and the permeability increased from 525.4 mD to 747.7 mD compared to specimen No.27. When printing specimen No.32, the material flow was increased from 0.85 to 0.9 compared to specimen No.27. As a result, the porosity of specimen No.32 decreased from 18.2% to 13.5% and the permeability from 525.4 mD to 442.3 mD compared to specimen No.27. A similar pattern is also seen in the comparison of specimens No.37 and No.27, No.39 and No.37, and No.31 and No.46.

The printing results showed that as the material flow or overlap percentage decreases, the porosity and permeability of the specimens increase. The porosity and permeability of the specimens decrease when the material flow or overlap percentage increases. For the material flow, the same pattern was demonstrated earlier in Tables 2–5, and was as expected.

Overlap percentage and material flow correlate. Changing the material flow changes the width of the material filament for both the infill and the outer wall, resulting in a change in the magnitude of overlap between them. Software-specified changes in the percentage of overlap can increase or decrease this effect.

Table 7 shows the printing results for specimens Nos.27–46 as a matrix where the porosity index of the specimens corresponds to the values of the material flow and the percentage of overlap with which the specimens were manufactured.

Table 7. Porosity of specimens at a given material flow and percentage of overlap.

		Flow of Material, d.u.							Porosity, %
		0.8	0.82	0.83	0.85	0.87	0.88	0.9	
Overlapping, %	20				20.1				12.8
	25				18.2			13.5	
	30						12.7		
	35					11.6			
	40	17.5			11.5				
	45			11.9					
	50		10.6						
Legend		20 (max)					10 (min)		%

Table 8 shows the results of printing specimens Nos.27–46 as a matrix, where the permeability index of the specimen corresponds to the values of the material flow and the percentage of overlap with which the specimens were produced.

Table 8. Permeability of specimens at a given material flow and percentage of overlap.

		Flow of Material, d.u.							Permeability, mD
		0.8	0.82	0.83	0.85	0.87	0.88	0.9	
Overlapping, %	20				747.7				337.8
	25				525.4			442.3	
	30						418.0		
	35					341.2			
	40	680.5			335.4				
	45			485.7					
	50		427.2						
Legend		750 (max)					330 (min)		mD

Tables 7 and 8 show that by increasing material flow and simultaneously reducing the percentage of overlap, an increase in effective porosity and a decrease in permeability can be achieved. And vice versa, by increasing the overlap percentage and simultaneously decreasing the material flow, a decrease in effective porosity can be achieved while increasing the permeability. When printing specimen No.46, the material flow was increased from 0.82 to 0.92 and the overlap percentage was reduced from 50% to 20% compared to specimen No.42. As a result, the porosity of specimen No.46 increased from 10.6% to 12.8% and the permeability decreased from 427.2 mD to 337.8 mD compared to specimen No.42.

Based on the information presented in Tables 7 and 8, it can be concluded that the dependence of porosity and permeability of the specimens on material flow and overlap percentage has a wave-like nature. The plots of dependence of the porosity and permeability of the specimens on the FFF 3D printing parameters are shown in Figure 7.

The possibility to vary the width of the material filament and the percentage of overlap between the infill and the outer wall is not unique to FFF 3D printing. Understanding the nature of this dependence can provide the possibility of flexible control of the porosity and permeability of synthetic specimens and facilitate the achievement of the desired performance when reconstructing the pore space of rocks (or other porous media) using different 3D printing technologies.

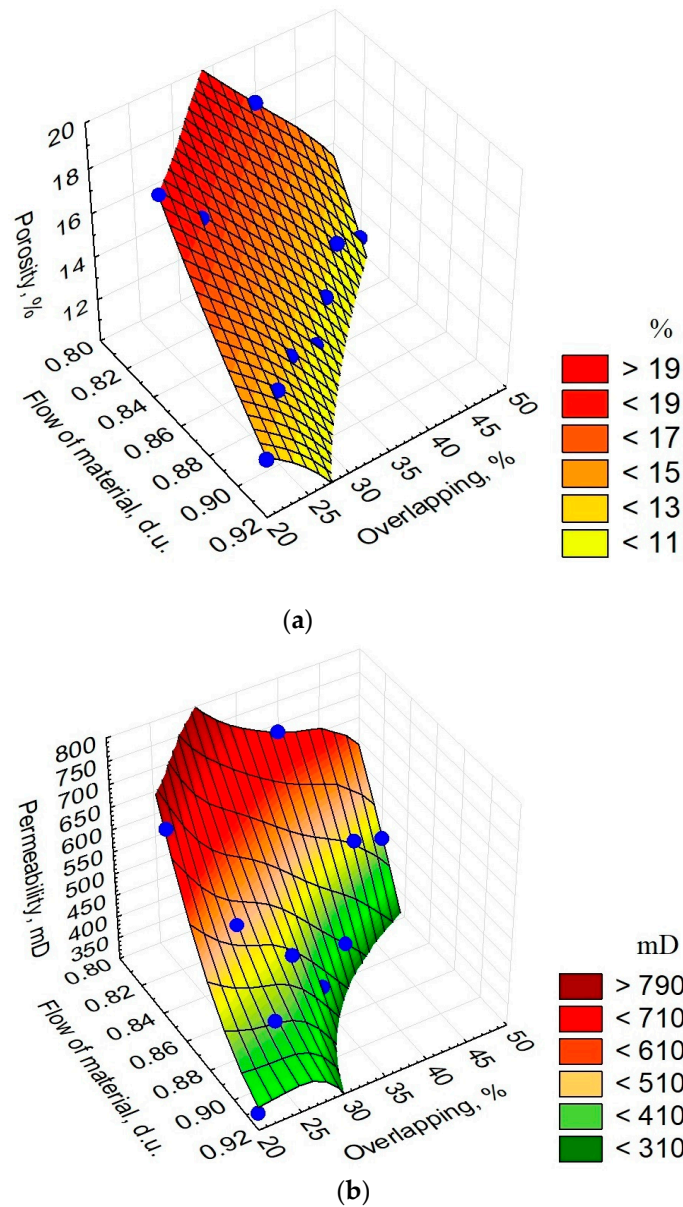


Figure 7. Plots of dependence of the porosity and permeability of the specimens on the FFF 3D printing parameters: (a) dependence of porosity on material flow and percentage of overlap; (b) dependence of permeability on material flow and percentage of overlap.

To better understand the nature of the obtained dependence, a more detailed study of FFF 3D printing of PLA specimens, fabrication of synthetic core specimens of other types (limestone, clay, shale, etc.), from different materials, and using different 3D printing technologies is required.

As a result of this study, two synthetic specimens were produced with porosity and permeability values extremely close to those of the original core (14% and 271 mD). The porosity of specimen No.32 was 13.5% and permeability was 442.3 mD. The porosity of specimen No.46 was 12.8% and permeability was 337.8 mD.

Thus, it is possible to reconstruct the pore space of the core in real-size using FFF 3D printing with sufficiently high accuracy. The obtained dependence pattern (Figure 7) indicates the possibility of a further reduction of the error in reconstructing the porosity and permeability of the core by changing the parameters of FFF 3D printing. The demonstrated results (specimens No.32, No.46) were achieved at the lowest printing resolution ($l_{xy} = 0.3 \text{ mm}$, $l_z = 0.1 \text{ mm}$). The printing results given in Tables 3–5 justify an assumption

that if other combinations of l_{xy} and l_z were used, the desired porosity and permeability values could have also been achieved. In addition, the combinations of l_{xy} and l_z provided for higher printing resolution can be used to reproduce the structure of other rock types (limestones, clays, shales, etc.).

4. Conclusions

An approach to the real-size reconstruction of porous media with given (target) porosity and permeability by controlling the parameters of FFF 3D printing using CT images of the original core is proposed. Real-size synthetic core specimens were manufactured on the basis of CT images by means of FFF 3D printing. The possibility of reconstructing the reservoir properties of sandstone cores was demonstrated. The results of gas porometry measurements showed that the porosity of specimens No.32 and No.46 was 13.5% and 12.8%, and permeability was 442.3 mD and 337.8 mD, respectively. The porosity of the original core was 14% and permeability was 271 mD.

In the course of this research, it has been shown that controlling the FFF 3D printing parameters allows us to create structures with different (target) porosity and permeability parameters.

It was found that changing the layer height and nozzle diameter, as well as the retract and restart distances, has a direct effect on the porosity and permeability of synthetic specimens. An increase in the nozzle diameter or layer height leads to a decrease in porosity and permeability. At low temperatures T_{ext} , the use of retracts and restarts with increased plastic feed led to clogging of pores and channels. In other words, as the restart distance increases, the porosity and permeability of the specimens decrease.

The dependence of the porosity and permeability of synthetic specimens on the flow (volumetric flow rate) of the material and the percentage of overlap between the infill and the outer wall during FFF 3D printing was revealed. The printing results showed that as the material flow or overlap percentage decreases, the porosity and permeability of the specimens increase. The porosity and permeability of the specimens decrease when the material flow or overlap percentage increases. At the same time, by increasing material flow and simultaneously reducing the percentage of overlap, an increase in effective porosity and a decrease in permeability can be achieved. And vice versa, by increasing the overlap percentage and simultaneously decreasing the material flow, a decrease in effective porosity can be achieved while increasing the permeability.

Understanding the nature of this dependence can provide the possibility of flexible control of porosity and permeability of synthetic specimens and facilitate the achievement of the desired performance when reconstructing the pore space of rocks (or other porous media) by different 3D printing technologies.

To better understand the nature of the obtained dependence, a more detailed study of FFF 3D printing of PLA specimens, fabrication of synthetic core specimens of other types (limestone, clay, shale, etc.), from different materials, and using different 3D printing technologies is required.

The obtained results will be used to create synthetic core specimens from thermoplastic composites with natural filling and from materials based on natural components.

Author Contributions: Conceptualization, A.A.O., A.A.K. and S.N.K.; methodology, A.A.O., A.A.K. and S.N.K.; software, A.A.O. and A.A.K.; validation, A.A.O. and Y.V.S.; formal analysis, A.A.O.; investigation, A.A.O. and Y.V.S.; resources, A.A.K., S.N.K. and A.A.O.; data curation, A.A.O.; writing—original draft preparation, A.A.O. and A.A.K.; writing—review and editing, A.A.O., A.A.K. and S.N.K.; visualization, A.A.K., Y.V.S. and A.A.O.; supervision, S.N.K.; project administration, S.N.K.; funding acquisition, A.A.K. All authors have read and agreed to the published version of the manuscript.

Funding: This research was funded by Russian Science Foundation, grant No. 22-77-00078.

Data Availability Statement: The data presented in this study are available on request from the corresponding author. The data are not publicly available due to the fact that further study will be carried out using the same data.

Conflicts of Interest: The authors declare no conflicts of interest.

References

1. Ishutov, S.; Jobe, T.D.; Zhang, S.; Gonzalez, M.; Agar, S.M.; Hasiuk, F.J.; Watson, F.; Geiger, S.; Mackay, E.; Chalaturnyk, R. Three-dimensional printing for geoscience: Fundamental research, education, and applications for the petroleum industry. *Am. Assoc. Pet. Geol. Bull.* **2018**, *102*, 1–26. [[CrossRef](#)]
2. Gao, Y.; Wu, T.; Zhou, Y. Application and prospective of 3D printing in rock mechanics: A review. *Int. J. Miner. Metall. Mater.* **2021**, *28*, 1–17. [[CrossRef](#)]
3. Niu, Q.; Jiang, L.; Li, C.; Zhao, Y.; Wang, Q.; Yuan, A. Application and prospects of 3d printing in physical experiments of rock mass mechanics and engineering: Materials, methodologies and models. *Int. J. Coal Sci. Technol.* **2023**, *10*, 5. [[CrossRef](#)]
4. Tan, W.; Wang, P. Experimental study on seepage properties of jointed rocklike samples based on 3D printing techniques. *Adv. Civ. Eng.* **2020**, *2020*, 10.
5. Xia, Y.; Meng, Q.; Zhang, C. Application of 3D Printing Technology in the Mechanical Testing of Complex Structural Rock Masses. *Geofluids* **2021**, *2021*, 7278131. [[CrossRef](#)]
6. Jiang, C.; Zhao, G.F. A Preliminary Study of 3D Printing on Rock Mechanics. *Rock Mech. Rock Eng.* **2014**, *48*, 1041–1050. [[CrossRef](#)]
7. Jiang, Q.; Feng, X.; Song, L.; Gong, Y.; Zheng, H.; Cui, J. Modeling rock specimens through 3D printing: Tentative experiments and prospects. *Acta Mech. Sin.* **2016**, *32*, 101–111. [[CrossRef](#)]
8. Huang, M.; Hong, C.; Sha, P.; Du, S.; Luo, Z.; Tao, Z. Method for visualizing the shear process of rock joints using 3D laser scanning and 3D printing techniques. *J. Rock Mech. Geotech. Eng.* **2023**, *15*, 204–215. [[CrossRef](#)]
9. Chen, X.; Zhang, Z.; Gao, J.; Kang, H. Study on Sustainable Development of Carbonate Reservoir Based on 3D Printing Technology. *Strateg. Plan. Energy Environ.* **2023**, *42*, 331–352. [[CrossRef](#)]
10. Almetwally, A.G.; Jabbari, H. 3D-Printing Replication of Porous Media for Lab-Scale Characterization Research. *ACS Omega* **2021**, *6*, 2655–2664. [[CrossRef](#)]
11. Jiang, Q.; Feng, X.; Gong, Y.; Song, L.; Ran, S.; Cui, J. Reverse modelling of natural rock joints using 3D scanning and 3D printing. *Comput. Geotech.* **2016**, *73*, 210–220. [[CrossRef](#)]
12. Song, L.; Jiang, Q.; Shi, Y.; Feng, X.; Li, Y.; Su, F.; Liu, C. Feasibility investigation of 3D printing technology for geotechnical physical models: Study of tunnels. *Rock Mech. Rock Eng.* **2018**, *51*, 2617–2637. [[CrossRef](#)]
13. Neumann, R.F.; Barsi-Andreeta, M.; Lucas-Oliveira, E.; Barbalho, H.; Trevizan, W.A.; Bonagamba, T.J.; Steiner, M.B. High accuracy capillary network representation in digital rock reveals permeability scaling functions. *Sci. Rep.* **2021**, *11*, 11370. [[CrossRef](#)] [[PubMed](#)]
14. Ardila, N.; Zambrano-Narvaez, G.; Chalaturnyk, R. Wettability Measurements on 3D Printed Sandstone Analogues and Its Implications for Fluid Transport Phenomena. *Transp. Porous Media* **2019**, *129*, 521–539. [[CrossRef](#)]
15. Gomez, J.; Chalaturnyk, R.; Zambrano-Narvaez, G. Experimental Investigation of the Mechanical Behavior and Permeability of 3D Printed Sandstone Analogues Under Triaxial Conditions. *Transp. Porous Media* **2019**, *129*, 541–557. [[CrossRef](#)]
16. Zhao, X.; Liu, Y.; Zou, C.; He, L.; Che, P.; Li, J. Physical Simulation of Brittle Rocks by 3D Printing Techniques Considering Cracking Behaviour and Permeability. *Appl. Sci.* **2024**, *14*, 344. [[CrossRef](#)]
17. Kong, L.; Ostadhassan, M.; Li, C.; Tamimi, N. Pore characterization of 3D-printed gypsum rocks: A comprehensive approach. *J. Mater. Sci.* **2018**, *53*, 5063–5078. [[CrossRef](#)]
18. Kong, L.; Ostadhassan, M.; Li, C.; Tamimi, N. Can 3-D Printed Gypsum Samples Replicate Natural Rocks? An Experimental Study. *Rock Mech. Rock Eng.* **2018**, *51*, 3061–3074. [[CrossRef](#)]
19. Kim, G.B.; Lee, S.; Kim, H.; Yang, D.H.; Kim, Y.H.; Kyung, Y.S.; Kim, C.S.; Choi, S.H.; Kim, B.J.; Ha, H.; et al. Three-dimensional printing: Basic principles and applications in medicine and radiology. *Korean J. Radiol.* **2016**, *17*, 182–197. [[CrossRef](#)]
20. Dizon, J.R.C.; Espera, A.H.; Chen, Q.; Advincula, R.C. Mechanical characterization of 3D-printed polymers. *Addit. Manuf.* **2018**, *20*, 44–67. [[CrossRef](#)]
21. Elkaseer, A.; Schneider, S.; Scholz, S.G. Experiment-Based Process Modeling and Optimization for High-Quality and Resource-Efficient FFF 3D Printing. *Appl. Sci.* **2020**, *10*, 2899. [[CrossRef](#)]
22. Kantaros, A.; Soulis, E.; Petrescu, F.I.T.; Ganetsos, T. Advanced Composite Materials Utilized in FDM/FFF 3D Printing Manufacturing Processes: The Case of Filled Filaments. *Materials* **2023**, *16*, 6210. [[CrossRef](#)]
23. Kochnev, A.A.; Krivoschekov, S.N. Paleontological studies using X-ray tomography. *Master's J.* **2015**, *2*, 177–181.
24. Krivoschekov, S.N.; Kochnev, A.A. Determination of capacitive properties of reservoir rocks using X-ray core tomography. *Master's J.* **2014**, *1*, 120–128.
25. Zinatullina, I.P.; Kadyrova, L.B. Lithological features of terrigenous reservoir rocks of the Viseian stage for development on the western slope of the South Tatar arch. In *Advances, Problems and Prospects of Oil and Gas Industry Development*; Almeteyevsk State Oil Institute: Almeteyevsk, Russia, 2018; pp. 106–112.

26. Almetwally, A.; Jabbari, H. Experimental investigation of 3D printed rock samples replicas. *J. Nat. Gas Sci. Eng.* **2020**, *76*, 103192. [[CrossRef](#)]
27. Ishutov, S.; Hodder, K.; Chalaturnyk, R.; Narvaez, G. Replication of carbonate reservoir pores at the original size using 3D printing. *Petrophysics* **2021**, *62*, 477–485. [[CrossRef](#)]
28. Hodder, K.J.; Nychka, J.A.; Chalaturnyk, R.J. Process limitations of 3D printing model rock. *Prog. Addit. Manuf.* **2018**, *3*, 173–182. [[CrossRef](#)]
29. Ibrahim, E.; Jouini, M.; Bouchaala, F.; Gomes, J. Simulation and Validation of Porosity and Permeability of Synthetic and Real Rock Models Using Three-Dimensional Printing and Digital Rock Physics. *ACS Omega* **2021**, *6*, 31775–31781. [[CrossRef](#)]
30. Hodder, K.J.; Sanchez-Barra, A.J.; Ishutov, S.; Zambrano-Narvaez, G.; Chalaturnyk, R.J. Increasing Density of 3D-Printed Sandstone through Compaction. *Energies* **2022**, *15*, 1813. [[CrossRef](#)]
31. Song, R.; Wang, Y.; Sun, S.; Liu, J. Characterization and microfabrication of natural porous rocks: From micro-CT imaging and digital rock modelling to micro-3D-printed rock analogs. *J. Pet. Sci. Eng.* **2021**, *205*, 108827. [[CrossRef](#)]
32. Hodder, K.; Craplewe, K.; Ishutov, S.; Chalaturnyk, R. Binder saturation as a controlling factor for porosity variation in 3D-printed sandstone. *Petrophysics* **2021**, *62*, 450–462. [[CrossRef](#)]
33. Robin, M.; Combes, R.; Degreve, F.; Cuiec, L. Wettability of porous media from Environmental Scanning Electron Microscopy: From model to reservoir rocks. In Proceedings of the International Symposium on Oilfield Chemistry, Houston, TX, USA, 18–21 February 1997; Society of Petroleum Engineers: Richardson, TX, USA, 1997.
34. Song, R.; Wang, Y.; Ishutov, S.; Zambrano-Narvaez, G.; Hodder, K.; Chalaturnyk, R.J.; Sun, S.; Liu, J.; Gamage, R. A Comprehensive Experimental Study on Mechanical Behavior, Microstructure and Transport Properties of 3D-printed Rock Analogs. *Rock Mech. Rock Eng.* **2020**, *53*, 5745–5765. [[CrossRef](#)]
35. Cheung, C.S.N.; Baud, P.; Wong, T. Effect of grain size distribution on the development of compaction localization in porous sandstone. *Geophys. Res. Lett.* **2012**, *39*, L21302. [[CrossRef](#)]
36. Ratnikov, I.; Yarkova, N.; Romanov, E. Analysis of Hydrocarbon Saturation Nature in a Heterogeneous Reservoir as Exemplified in AC10 Formation of Priobskoe Field. *Min. Sci. Technol.* **2019**, *4*, 42–56. [[CrossRef](#)]
37. Chilingar, G.V. Relationship between Porosity, Permeability, and Grain-Size Distribution of Sands and Sandstones. *Dev. Sedimentol. Deltaic Shallow Mar. Depos.* **1964**, *1*, 71–75.
38. Valeeva, S.E.; Baranova, A.G.; Uspenskiy, B.V. Influence of sedimentation conditions on formation of reservoir rocks of Bobrikovoradayeyskaya sediments. *Scient. Nat. Sci. Ser.* **2015**, *157*, 60–72.
39. Ishibashi, T.; Fang, Y.; Elsworth, D.; Watanabe, N.; Asanuma, H. Hydromechanical properties of 3D printed fractures with controlled surface roughness: Insights into shear-permeability coupling processes. *Int. J. Rock Mech. Min. Sci.* **2020**, *128*, 104271. [[CrossRef](#)]
40. Bacher, M.; Schwen, A.; Koestel, J. Three-Dimensional Printing of Macropore Networks of an Undisturbed Soil Sample. *Vadose Zone J.* **2015**, *14*, 1–10. [[CrossRef](#)]
41. Ishutov, S.; Hasiuk, F.J.; Jobe, D.; Agar, S. Using Resin-Based 3D Printing to Build Geometrically Accurate Proxies of Porous Sedimentary Rocks. *Groundwater* **2018**, *56*, 482–490. [[CrossRef](#)]
42. Ishutov, S.; Hasiuk, F. 3D printing Berea sandstone: Testing a new tool for petrophysical analysis of reservoirs. *Petrophysics* **2017**, *58*, 592–602.
43. Jouini, M.S.; Gomes, J.S.; Tembely, M.; Ibrahim, E.R. Upscaling Strategy to Simulate Permeability in a Carbonate Sample Using Machine Learning and 3D Printing. *IEEE Access* **2021**, *9*, 90631–90641. [[CrossRef](#)]
44. Fahim Salek, M.; Shinde, V.V.; Beckingham, B.S.; Beckingham, L.E. Resin based 3D printing for fabricating reactive porous media. *Mater. Lett.* **2022**, *322*, 132469. [[CrossRef](#)]
45. Kanjirakat, A.; Carvero, A.; Amani, M.; Retnanto, A. Surface modification of stereolithography-based 3D printed structures utilizing ultrasonic-atomised sprays. *J. Mater. Sci.* **2023**, *58*, 6931–6943. [[CrossRef](#)]
46. Ishutov, S.; Hasiuk, F.; Harding, C.; Gray, J.N. 3D printing sandstone porosity models. *Interpretation* **2015**, *3*, SX49–SX61. [[CrossRef](#)]
47. Goral, J.; Deo, M. Nanofabrication of synthetic nanoporous geomaterials: From nanoscale-resolution 3D imaging to nano-3D-printed digital (shale) rock. *Sci. Rep.* **2020**, *10*, 21596. [[CrossRef](#)] [[PubMed](#)]
48. Ishutov, S.; Hasiuk, F.J.; Fullmer, S.M.; Buono, A.S.; Gray, J.N.; Harding, C. Resurrection of a reservoir sandstone from tomographic data using three-dimensional printing. *Am. Assoc. Pet. Geol. Bull.* **2017**, *101*, 1425–1443. [[CrossRef](#)]
49. Kong, L.; Ostadhassan, M.; Hou, X.; Mann, M.; Li, C. Microstructure characteristics and fractal analysis of 3D-printed sandstone using micro-CT and SEM-EDS. *J. Pet. Sci. Eng.* **2019**, *175*, 1039–1048. [[CrossRef](#)]
50. Ardila, N. Hydraulic Properties Characterization of 3D Printed Sandstone Analogues. Master's Thesis, University of Alberta, Edmonton, AB, Canada, 2018.
51. Wang, Y.; Li, S.; Song, R.; Liu, J.; Ye, M.; Peng, S.; Deng, Y. Effects of Grain Size and Layer Thickness on the Physical and Mechanical Properties of 3D-Printed Rock Analogs. *Energies* **2022**, *15*, 7641. [[CrossRef](#)]
52. Mechtcherine, V.; Bos, F.P.; Perrot, A.; da Silva, W.R.L.; Nerella, V.N.; Fataei, S.; Wolfs, R.J.M.; Sonebi, M.; Roussel, N. Extrusion-based additive manufacturing with cement-based materials—Production steps, processes, and their underlying physics: A review. *Cem. Concr. Res.* **2020**, *132*, 106037. [[CrossRef](#)]
53. Rehman, A.U.; Kim, J.H. 3D Concrete Printing: A Systematic Review of Rheology, Mix Designs, Mechanical, Microstructural, and Durability Characteristics. *Materials* **2021**, *14*, 3800. [[CrossRef](#)]

54. Yu, S.; Xia, M.; Sanjayan, J.; Yang, L.; Xiao, J.; Du, H. Microstructural Characterization of 3D Printed Concrete. *J. Build. Eng.* **2021**, *44*, 102948. [[CrossRef](#)]
55. Feng, X.T.; Gong, Y.H.; Zhou, Y.Y.; Li, Z.W.; Liu, X.F. The 3D-printing technology of geological models using rock-like materials. *Rock Mech. Rock Eng.* **2019**, *52*, 2261–2277. [[CrossRef](#)]
56. Shi, X.; Deng, T.; Lin, S.; Zou, C.; Liu, B. Method of fabricating artificial rock specimens based on extrusion free forming (EFF) 3D printing. *J. Rock Mech. Geotech. Eng.* **2023**, *16*, 1455–1466. [[CrossRef](#)]
57. Shigueoka, M.O.; de M Junqueira, S.L.; Alves, T.A.; Volpato, N. Permeability Analysis of Polymeric Porous Media Obtained by Material Extrusion Additive Manufacturing. In Proceedings of the 30th Annual International Solid Freeform Fabrication Symposium—An Additive Manufacturing Conference, University of Texas at Austin, Austin, TX, USA; 2019.
58. Shigueoka, M.; Volpato, N. Expanding manufacturing strategies to advance in porous media planning with material extrusion additive manufacturing. *Addit. Manuf.* **2020**, *38*, 101760. [[CrossRef](#)]
59. Huang, L.; Stewart, R.; Dyaar, N.; Baez-Franceschi, J. 3D-printed rock models: Elastic properties and the effects of penny-shaped inclusions with fluid substitution. *Geophysics* **2016**, *81*, D669–D677. [[CrossRef](#)]
60. Anjekar, I.S.; Wales, S.; Beckingham, L.E. Fused Filament Fabrication 3-D Printing of Reactive Porous Media. *Geophys. Res. Lett.* **2020**, *47*, e2020GL087665. [[CrossRef](#)]
61. Zhou, T.; Zhu, J.B. Application of 3D printing and micro-CT scan to rock dynamics. In Proceedings of the ISRM International Conference on Rock Dynamics, Suzhou, China, 18–19 May 2016.
62. Liu, P.; Ju, Y.; Ranjith, P.; Zheng, Z.; Wang, L.; Wanniarachchi, A. Visual representation and characterization of three-dimensional hydrofracturing cracks within heterogeneous rock through 3D printing and transparent models. *Int. J. Coal Sci. Technol.* **2016**, *3*, 284–294. [[CrossRef](#)]
63. Galkin, S.V.; Efimov, A.A.; Krivoshechekov, S.N.; Savitsky, Y.V.; Cherepanov, S.S. Application of X-ray tomography method in petrophysical studies of oil and gas field core. *Geol. Geophys.* **2015**, *56*, 995–1007.
64. Savitsky, Y.V. Modern Possibilities of X-ray tomography method in study of oil and gas fields' core. *Vestn. Perm Natl. Res. Polytech. University. Geol. Oil Gas Min. Eng.* **2015**, *15*, 28–37.
65. PrintProduct PLA. Available online: <https://printproduct3d.ru/catalog.html#/PLA-GEO-%D0%BF%D0%BB%D0%B0%D1%81%D1%82%D0%B8%D0%BA-PrintProduct/p/82308141/category=34105291> (accessed on 18 April 2024).
66. Wolszczak, P.; Lygas, K.; Paszko, M.; Wach, R.A. Heat distribution in material during fused deposition modelling. *Rapid Prototyp. J.* **2018**, *24*, 615–622. [[CrossRef](#)]
67. Vanaei, H.; Shirinbayan, M.; Deligant, M.; Raissi, K.; Fitoussi, J.; Khelladi, S.; Tcharkhtchi, A. Influence of process parameters on thermal and mechanical properties of polylactic acid fabricated by fused filament fabrication. *Polym. Eng. Sci.* **2020**, *60*, 1822–1831. [[CrossRef](#)]
68. Shahriar, B.B.; France, C.; Valerie, N.; Arthur, C.; Christian, G. Toward improvement of the properties of parts manufactured by FFF (fused filament fabrication) through understanding the influence of temperature and rheological behaviour on the coalescence phenomenon. *AIP Conf. Proc.* **2017**, *1896*, 040008.
69. Sun, Q.; Rizvi, G.M.; Bellehumeur, C.T.; Gu, P. Effect of processing conditions on the bonding quality of FDM polymer filaments. *Rapid Prototyp. J.* **2008**, *14*, 72–80. [[CrossRef](#)]
70. Haq, R.H.A.; Marwah, O.F.; Rahman, M.A.; Haw, H.F.; Abdullah, H.; Ahmad, S. 3D Printer parameters analysis for PCL/PLA filament wire using Design of Experiment (DOE). *Mater. Sci. Eng.* **2019**, *607*, 012001.
71. Oskolkov, A.A.; Bezukladnikov, I.I.; Trushnikov, D.N. Mathematical Model of the Layer-by-Layer FFF/FGF Polymer Extrusion Process for Use in the Algorithm of Numerical Implementation of Real-Time Thermal Cycle Control. *Polymers* **2023**, *15*, 4518. [[CrossRef](#)]
72. Vanaei, H.R.; Raissi, K.; Deligant, M.; Shirinbayan, M.; Fitoussi, J.; Khelladi, S.; Tcharkhtchi, A. Toward the understanding of temperature effect on bonding strength, dimensions and geometry of 3D-printed parts. *J. Mater. Sci.* **2020**, *55*, 14677–14689. [[CrossRef](#)]
73. Davis, C.S.; Hillgartner, K.E.; Han, S.H.; Seppala, J.E. Mechanical strength of welding zones produced by polymer extrusion additive manufacturing. *Addit. Manuf.* **2017**, *16*, 162–166. [[CrossRef](#)]
74. Seppala, J.E.; Han, S.H.; Hillgartner, K.E.; Davis, C.S.; Migler, K.B. Weld formation during material extrusion additive manufacturing. *Soft Matter* **2017**, *13*, 6761–6769. [[CrossRef](#)]
75. Aliheidari, N.; Christ, J.; Tripuraneni, R.; Nadimpalli, S.; Ameli, A. Interlayer adhesion and fracture resistance of polymers printed through melt extrusion additive manufacturing process. *Mater. Des.* **2018**, *156*, 351–361. [[CrossRef](#)]

Disclaimer/Publisher's Note: The statements, opinions and data contained in all publications are solely those of the individual author(s) and contributor(s) and not of MDPI and/or the editor(s). MDPI and/or the editor(s) disclaim responsibility for any injury to people or property resulting from any ideas, methods, instructions or products referred to in the content.